PHILOSOPHICAL TRANSACTIONS A

royalsocietypublishing.org/journal/rsta

Research

Cite this article: Chapman M, De Graef M, James RD Chen X. 2021 Quantitative analysis of compatible microstructure by electron backscatter diffraction. *Phil. Trans. R. Soc. A* **379**: 20200112.
https://doi.org/10.1098/rsta.2020.0112

Accepted: 15 December 2020

One contribution of 10 to a theme issue 'Topics in mathematical design of complex materials'.

Subject Areas:
crystallography, materials science

Keywords:
electron backscatter diffraction, martensite, compatibility, microstructure

Author for correspondence:
Xian Chen
e-mail: xianchen@ust.hk

Downloaded from https://royalsocietypublishing.org/ on 14 July 2022

Quantitative analysis of compatible microstructure by electron backscatter diffraction

Michael Chapman[1,2], Marc De Graef[1], Richard D. James[3] and Xian Chen[4]

[1]Materials Science and Engineering, Carnegie Mellon University, PA 15213, USA
[2]UES, Inc. Dayton, OH 45432, USA
[3]Aerospace Engineering and Mechanics, University of Minnesota, MN 55455, USA
[4]Mechanical and Aerospace Engineering, Hong Kong University of Science and Technology, Hong Kong

MC, 0000-0002-2926-0303; XC, 0000-0002-0114-4642

We propose a scheme for assigning the martensite variant using electron backscatter diffraction in a martensite material that undergoes a solid–solid phase transformation. Based on the solutions of the crystallographic equations of martensite, we provide an algorithm to assign martensite variants to a particular microscopic region, and to check the elastic compatibility of the microstructure corresponding to low hysteresis and high reversibility in shape memory alloys.

This article is part of the theme issue 'Topics in mathematical design of complex materials'.

1. Introduction

Martensitic transformations are diffusionless structural phase transformations that have been widely observed in metals, alloys, ceramics and even crystalline polymers [1–4]. In metals, the martensitic transformation can be either irreversible, as seen in the quenching process of steel [5], or reversible, as seen in shape memory alloys [2]. Both types are characterized by a symmetry-breaking structural transformation accompanied by the formation of a rich microstructure. The mechanical properties, such as recoverable strain, stiffness and ductility, as well as some transport properties, such as conductivity, polarization and magnetization of

THE ROYAL SOCIETY PUBLISHING

© 2021 The Author(s) Published by the Royal Society. All rights reserved.

Downloaded from https://royalsocietypublishing.org/ on 14 July 2022

these transforming metals strongly depend on the morphological configurations of the martensite microstructure. Shape memory alloys are the primary family of the transforming metals, widely exploited for self-expandable stents, micro-actuation devices and solid-state refrigerators [6–8]. Among the most studied shape memory alloys, Nitinol (a slightly Ni-rich NiTi alloy) is the most successful one by a large margin because of its superior thermo-mechanical performance, i.e. about 5% superelastic strain has been achieved under 0.5 GPa stress at room temperature [6]. However, its advanced mechanical properties degrade quickly with an accumulation of large hysteresis and residual strains during cyclic transformations [9–11].

Based on heuristic assumptions and empirical rules from observation, in the early 1990s, the functional fatigue of shape memory alloys was believed to be related to a pinning mechanism caused by intrinsic defects, and a thermal activation mechanism caused by a time-dependent transformation path [12,13]. Thereafter, extensive work was performed on special heat treatments and compositional doping to reduce the hysteresis by eliminating pinning sites or facilitating the thermal activation; however, those metallurgical methods were not effective, and sometimes led to opposite effects. For instance, Lovey & Torra showed that the dislocations exhibit a paradoxical behaviour toward the size of the hysteresis of the martensitic transformation in a CuZnAl shape memory alloy [14]; Otsuka *et al.* proved experimentally that the size of hysteresis of CuAlNi during stress-induced martensitic transformations does not have strong strain rate dependence [15].

Almost simultaneously with the metallurgical developments, theories of rational mechanics and mathematics were applied to the study of the microstructure for martensitic phase transformation, based on the minimization of free energy [16–18]. In a solid–solid transformation with a change of crystal symmetry, a very fine mixture of twins of the martensite phase forms and is separated by a planar interface from the homogeneous austenite phase. For energetic reasons, the material in the austenitic state will be deformed into a sequence of states characterized by deformation gradients $\{\mathbf{I}, \mathbf{F}^+, \mathbf{F}^-\} \subset \mathbb{R}^{3\times 3}$, where $\mathbf{I}$ refers to the reference configuration, and the deformation gradients $\mathbf{F}^+\|\mathbf{F}^-\|\mathbf{F}^+\|\mathbf{F}^-$ represent a piecewise affine deformation comprised of martensite twin laminates. The sequence of deformation gradients needs to satisfy the kinematic condition of interface compatibility. That is, a *rank-one relation* of the form

$$\mathbf{F}^+ - \mathbf{F}^- = \mathbf{a} \otimes \mathbf{n} \tag{1.1}$$

for some vectors $\mathbf{a}, \mathbf{n} \in \mathbb{R}^3$; conventionally, $\mathbf{n}$ is the twinning plane normal and $\mathbf{a}$ is the twinning shear vector. The stretch parts of $\mathbf{F}^+$ and $\mathbf{F}^-$ are symmetry-related variants of martensite [3,17,19]. For most martensitic transformations, such as cubic-to-tetragonal, cubic-to-orthorhombic and cubic-to-monoclinic, the rank-one relation of twins is generic and underlies the microstructure of martensite. The condition of compatibility between $\mathbf{I}$ and either $\mathbf{F}^+$, $\mathbf{F}^-$ does not necessarily hold, but it has been shown by a weak convergence theorem [16] that the mixture of deformation gradients $\mathbf{F}^+$ and $\mathbf{F}^-$ can be compatible with $\mathbf{I}$ if the mixture gets finer and finer at the interface. The calculations of the interface between the homogeneous austenite and the fine mixture of martensite variants are related closely to the results given by the phenomenological theory of martensite [20–23], and align with all experimental observations with remarkably good agreement [2,3,17,20,23,24]. Beyond the prediction of habit planes and martensite twinning structures, the mathematical theories developed on the basis of energy minimization provide a rational understanding of the origin of hysteresis in shape memory alloys [24–26]. A new mathematical theory based on Γ-convergence arguments [26] was proposed to calculate the size of the hysteresis as the energy barrier for the formation of twinned martensite from homogeneous austenite through elastic transition layers. It has been rigorously proven that the limiting energy barrier (that is, the least hysteresis) corresponds to the satisfaction of the condition $\lambda_2 = 1$, where λ_2 is the middle principal stretch of the transformation stretch tensor. Thus, the size of the hysteresis in shape memory alloys is minimized by satisfying a simple criterion $\lambda_2 = 1$ despite the presence of local defects, a rate-dependent transformation path and even a volume change.

Downloaded from https://royalsocietypublishing.org/ on 14 July 2022

Table 1. Nomenclature.

$\mathbf{s}_i, i = 1, 2, 3$	machine basis attached to the stage.
$\mathbf{e}_i^a, i = 1, 2, 3$	conventional lattice basis of austenite.
$\mathbf{e}_i^{(k)}, i = 1, 2, 3$	conventional lattice basis of martensite in the single variant region $\mathcal{R}_k$.
$\hat{\mathbf{e}}_i^a, i = 1, 2, 3$	sublattice vectors of austenite derived by lattice correspondence.
$\mathbf{p}_i, i = 1, 2, 3$	primitive basis of austenite.
$\gamma_i^j, i, j = 1, 2, 3$	transformation matrix that maps $\mathbf{e}_i^a$ to $\hat{\mathbf{e}}_i^a$.
$\boldsymbol{\Gamma}$	matrix presentation of $\bar{\gamma}_i^j$ in the cubic basis of crystal.
$\mathcal{R}_k, k = 1, \ldots, N$	sub-region occupied by a single variant of martensite.
$\mathcal{P}$	the point group of austenite.
$\mathbf{Q}_i, i = 1, \ldots, \lvert\mathcal{P}\rvert$	matrix representation of element in the point group of austenite.
$\mathbf{M}_i, i = 1, \ldots, \lvert\mathcal{P}\rvert$	matrix representation of element in the lattice group of austenite.
$\varphi_1^a, \Phi^a, \varphi_2^a$	Euler angles for austenite lattice, measured by electron backscatter diffraction (EBSD).
$\varphi_1^{(k)}, \Phi^{(k)}, \varphi_2^{(k)}$	Euler angles for martensite lattice in the region $\mathcal{R}_k$, measured by EBSD.
$\mathbf{O}_a$	orientation matrix of austenite.
$\mathbf{O}_m^{(k)}$	orientation matrix of martensite.
$\mathbf{F}_k$	the deformation gradient of the region $\mathcal{R}_k$.
$\mathbf{U}_\ell$	the transformation stretch tensor of the ℓth martensite variants where $\ell = 1, \ldots, \lvert\mathcal{P}\rvert/\lvert\mathcal{P}^m\rvert$.
$\mathbf{n}_0$	the surface normal of the specimen in austenite.

Geometrically, $\lambda_2 = 1$ guarantees a distortion-free interface between austenite and a single variant of martensite. The notations used in this paper are shown in table 1.

In a variety of alloy systems such as NiTiCu [24,27], NiTiPd [26,28], NiTiCuPd [29], and Heusler alloys NiCoMnSn [30] and NiCoMnIn [31], tuning the lattice parameters to achieve $\lambda_2 = 1$ at interfaces has been conclusively demonstrated as a successful development strategy for low-hysteresis shape memory alloys. The quantitative characterization of the compatible interface between austenite and a single variant of martensite was conducted under high-resolution transmission electron microscopy in an alloy family of NiTiPd with varying Pd compositions [32,33]. These experiments provide two important quantitative pieces of evidence for the relation between λ_2 and the morphology of martensite: (1) As the λ_2 value approaches 1, the martensite gradually becomes twinless; and (2), the austenite/martensite interface, characterized as $(7\bar{5}5)_{B2}$, satisfies the rank-one relation in (1.1) exactly between austenite and a single martensite variant.

Further compatibility conditions, known as the *cofactor conditions* (CC), can be derived for austenite and twinned martensite interfaces [26,28]. Beyond $(\mathrm{CC})_1 : \lambda_2 = 1$ where λ_2 is the middle eigenvalue of transformation stretch tensor $\mathbf{U}$, the cofactor conditions require two additional sub-conditions $(\mathrm{CC})_2 : \mathbf{a} \cdot \mathrm{cof}(\mathbf{U}^2 - \mathbf{I})\mathbf{n} = 0$; and $(\mathrm{CC})_3 : \mathrm{tr}\mathbf{U}^2 + \det \mathbf{U}^2 - (1/4)|\mathbf{a}|^2|\mathbf{n}|^2 \geq 2$ for certain twin systems with twinning plane normal $\mathbf{n}$ and twin shear vector $\mathbf{a}$. Let $\mathbf{U}$ and $\hat{\mathbf{U}}$ be the pair of variants of a certain twin laminate, where $\hat{\mathbf{U}} = (-\mathbf{I} + 2\mathbf{e} \otimes \mathbf{e})\mathbf{U}(-\mathbf{I} + 2\mathbf{e} \otimes \mathbf{e})$ for $\mathbf{e} \in \mathbb{R}^3$, $|\mathbf{e}| = 1$ being one of the twofold symmetry axes of the austenite lattice. The cofactor conditions are summarized in table 2 for Type-I, Type-II and Compound twin systems [28]. When a martensitic material satisfies all sub-conditions of the CC, it exhibits an unusual microstructure, observed as curved austenite/twinned martensite interfaces in $Cu_{25}Au_{30}Zn_{45}$ [34], and a profound enhancement of reversibility in both thermally and mechanically driven structural transformations [28, 35]. The quantitative characterization of $Cu_{25}Au_{30}Zn_{45}$was conducted by synchrotron X-ray microdiffraction (μSXRD) [36]. Using a temperature gradient stage, the austenite and martensite interface can be scanned by the micro beam of X-rays. Using the orientation relationship, the

Downloaded from https://royalsocietypublishing.org/ on 14 July 2022

Table 2. Cofactor conditions in different types of twin systems for the martensite variant **U** and the corresponding twofold symmetry axis **e** and its orthogonal vector $\mathbf{e}^{\perp} \cdot \mathbf{e} = 0$, $|\mathbf{e}^{\perp}| = 1$. The vector $\mathbf{v}_2$ is the normalized eigenvector of **U** associated with the middle eigenvalue λ_2 [28].

	$(CC)_1$	$(CC)_2$	$(CC)_3$
Type-I	$\lambda_2 = 1$	$\lvert\mathbf{U}^{-1}\mathbf{e}\rvert = 1$	satisfied
Type-II		$\lvert\mathbf{U}\mathbf{e}\rvert = 1$	
compound		$\mathbf{e} \cdot \mathbf{v}_2 = 0$ and $\mathbf{e}^{\perp} \cdot \mathbf{v}_2 = 0$	$(2\sqrt{1-(\mathbf{e} \cdot \mathbf{v}_2)^2(\mathbf{e}^{\perp} \cdot \mathbf{v}_2)^2} + 1) \det \mathbf{U}^2 \geq 2$

deformation gradient of a martensite variant can be measured. Thus, the orientation map of martensite phases can be converted to a deformation map, which provides important insights into the mechanical properties of the phase-transforming metal. However, the spatial resolution of microdiffraction is limited by the beam size and the scanning step size. The fine microstructure, specially the twin laminates of martensite, is difficult to be resolved by the micro beam of X-rays.

Similar to X-ray microdiffraction, the EBSD is a diffraction-based probe providing much higher spatial resolution. The EBSD technique is more suitable for the quantitative analysis of the crystallographic relations of twins at finer scales, e.g. the nano-scale martensitic twins of NiTi [37], the 5M [38] and 7M [39] modulated martensite twins within a grain of NiMnGa. In this paper, we introduce a method of quantitative determination of deformations of the highly reversible transforming metal $Cu_{25}Au_{30}Zn_{45}$ by EBSD, which enables sufficient spatial resolution (i.e. in the nanometre to submicrometre range) to resolve the fine martensite twins satisfying rank-one compatibility. Unlike X-ray probes, the electron probe cannot directly measure the lattice vectors *in situ* with varying temperature; thus we use continuum mechanics with application to geometric nonlinear theory of martensite to derive a general variant assignment method. As a result, we are able to convert the EBSD orientation map to a deformation map, by which the elastic compatibility and twinning parameters can be quantified.

2. Microstructure characterization by SEM with EBSD

We use the same piece of $Cu_{25}Au_{30}Zn_{45}$ prepared in reference [34] to study the compatible microstructure using the FEI Quanta 600 field emission scanning electron microscope equipped with an Oxford Instruments EBSD detector system and a liquid nitrogen cooling stage. The sample undergoes a reversible martensitic transformation at approximately −40°C driven by the installed cryogenic stage inside SEM. It was polished at room temperature in the austenitic phase, corresponding to the SEM image in figure 1*a*. Let the austenite be the reference configuration Ω_0; the deformation gradient of austenite is assigned to be **I** expressed in the cubic basis of the austenite lattice. As the temperature decreases through the phase transformation, the SEM images of martensite exhibit piecewise linear surface relief in figure 1*b–d*. Based on previous X-ray diffraction characterization, the symmetry of austenite is $Fm\bar{3}m$ (i.e. cubic $L2_1$) with lattice parameter $a_0 = 6.1606$ Å, and the symmetry of martensite is $P2_1$ (i.e. long modulated monoclinic M18R) with lattice parameters $a = 4.4580$ Å, $b = 5.7684$ Å, $c = 40.6980$ Å and $\beta = 86.80°$ [34,36].

Let the orthonormal basis $(\mathbf{s}_1, \mathbf{s}_2, \mathbf{s}_3)$ correspond to the transverse (TD), rolling (RD) and normal (ND) directions of SEM, defined as the machine basis. We consider a continuous deformation of the single domain (Ω_0) within a grain of austenite transforming to N regions $\mathcal{R}_1, \ldots \mathcal{R}_N$ containing variants of martensite. Figure 2 shows a grain of austenite with size of several millimetres scanned by EBSD. The orientation deviation within most of the grain is about 3° with a maximum deviation of 6.3°. The inverse pole ([001]) figure in figure 2*c* shows the averaged orientation of austenite. Upon continuous cooling, it transforms to martensite phase exhibiting much finer microstructures at approximately −40°C. We zoomed in an area of interest and conducted the EBSD scan. Consequently, we observed four sub-regions of martensite, $\mathcal{R}_i$, $i = 1, 2, 3, 4$ as shown in figure 3. The imaged microstructure in figure 3*a* is shifted a bit compared to the EBSD scanned

Downloaded from https://royalsocietypublishing.org/ on 14 July 2022

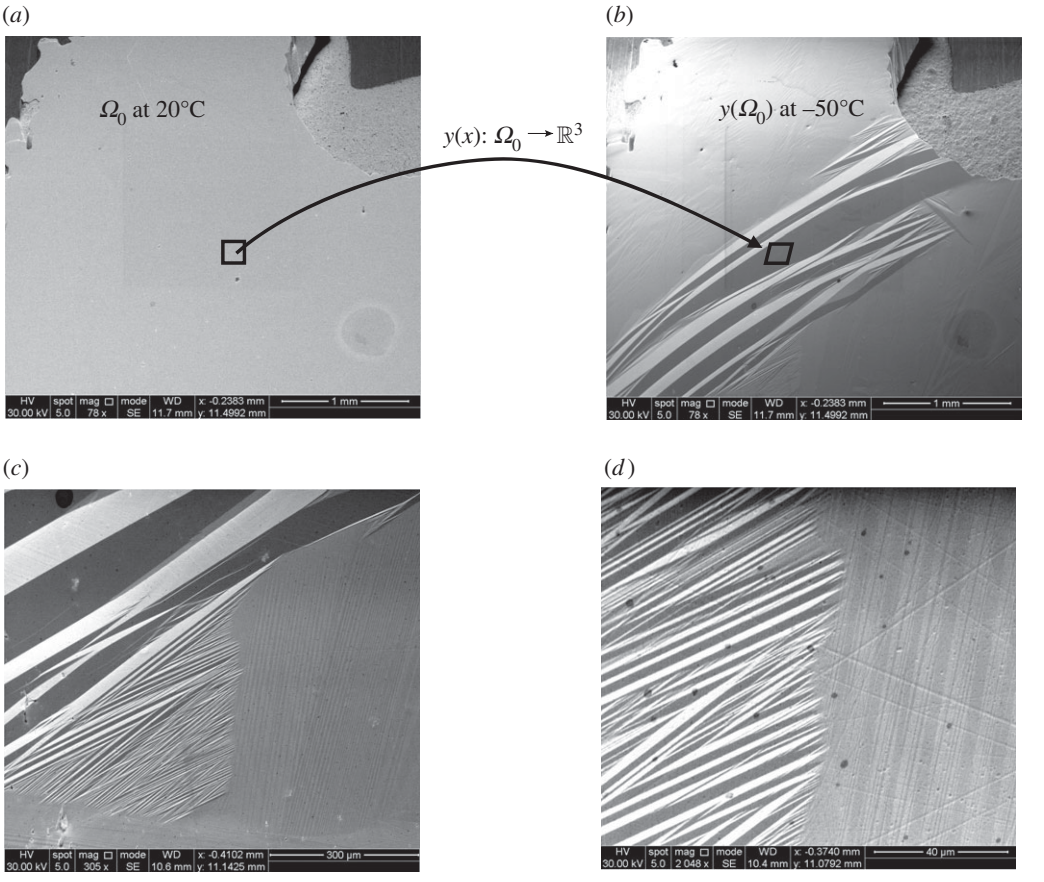

Figure 1. SEM images of (*a*) austenite phase at room temperature 20°C, (*b*)–(*d*) martensite phase at −50°C at different magnifications.

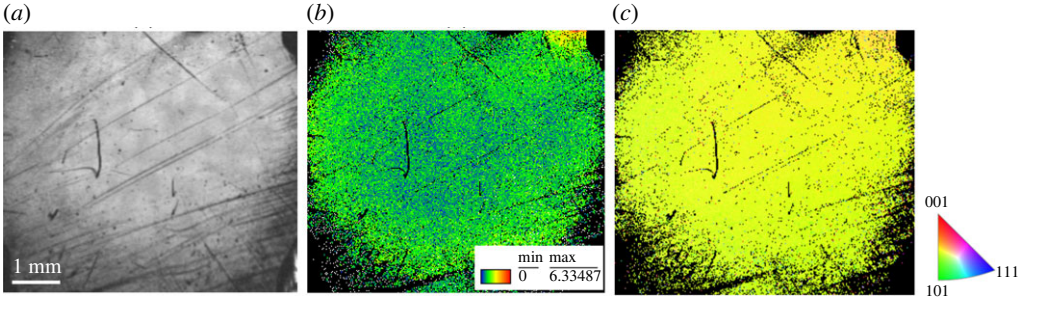

Figure 2. EBSD results of (*a*) austenite phase measured at room temperature corresponding to (*b*) Grain Reference Orientation Deviation (GROD) map with a maximum deviation of 6.3°, and (*c*) the orientation distribution of inverse pole figure map. (Online version in colour.)

region in figure 3*b*, where the martensite interfaces look slightly bent. This is due to the imaging distortion caused by thermal fluctuations during the long run of EBSD process.

Three Euler angles φ_1, Φ and φ_2 are measured by EBSD for a specific location x in the scanned region. With the information of the crystal symmetry and lattice parameters, we can calculate a linear transformation $\mathbf{O} \in \mathbb{R}^{3\times3}$, defined as the orientation matrix that maps the machine basis into

Downloaded from https://royalsocietypublishing.org/ on 14 July 2022

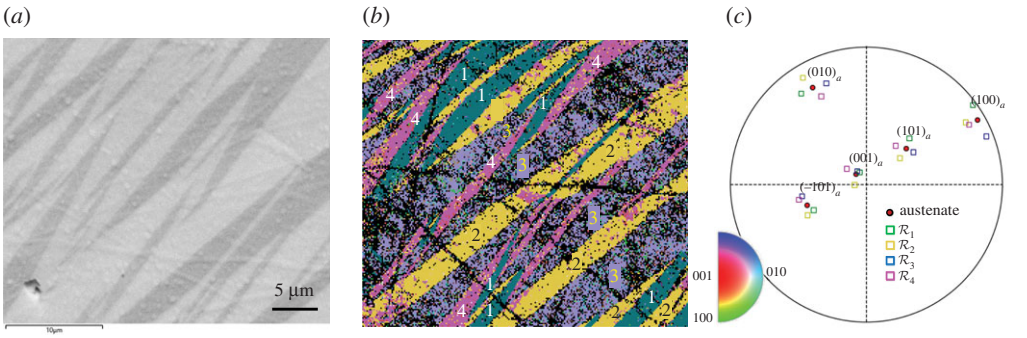

Figure 3. EBSD results of (*a*) martensite phase measured at approximately −40°C corresponding to (*b*) the orientation map showing four martensite sub-domains $\mathcal{R}_i$, $i = 1, 2, 3, 4$. (*c*) The stereographic projection of crystallographic relationships between the normals of $\{100\}_a$, $(101)_a$ and $(\bar{1}01)_a$ in austenite phase and in each of the martensite sub-domains. (Online version in colour.)

the conventional lattice basis of the crystal. Appendix A includes the calculations of the matrix representation of the orientation matrix from the crystallographic information. As illustrated in figure 4, the lattice bases of the different phases are related to the machine basis by

$$\mathbf{e}_i^a = \mathbf{O}_a \mathbf{s}_i, \ i = 1, 2, 3 \tag{2.1}$$

for the orientation matrix $\mathbf{O}_a$ in austenite region, and

$$\mathbf{e}_i^{(k)} = \mathbf{O}_m^{(k)} \mathbf{s}_i, \ i = 1, 2, 3 \tag{2.2}$$

for one of the orientation matrices $\mathbf{O}_m^k$ in the martensite region, $\mathcal{R}_k, k \in \{1, \ldots, N\}$. Because the basis vectors $\mathbf{s}_i$, $\mathbf{e}_i^a$ and $\mathbf{e}_i$ define a right-hand coordinate systems, the determinants of the orientation matrices satisfy

$$\det \mathbf{O}_a > 0 \quad \text{and} \quad \det \mathbf{O}_m^k > 0$$

for all $k = 1, \ldots, N$. Let $\mathbf{t}_{ij} \in \mathbb{R}^3$ be vectors that are parallel to the traces of the interfaces between regions $\mathcal{R}_i$ and $\mathcal{R}_j$ in martensite, projected onto the image plane. Assuming the microscope has been set up so that the image plane is parallel to the planar surface of austenite before transformation, then $\mathbf{t}_{ij} \cdot \mathbf{n}_0 = 0$ where $\mathbf{n}_0$ denotes the twinning interface normal in reference configuration (austenite). In general, the unprojected traces of interfaces will have various small out-of-plane components due to surface relief and the complex microstructure. Visually, the in-plane traces of the EBSD image look bent slightly due to the perspective effect. The components of these vectors are given in the machine basis. If the conventional lattice vectors do not vary substantially in a region, then, by the Cauchy–Born rule, the associated deformation gradient is constant in that region. Two neighbouring regions $\mathcal{R}_i$ and $\mathcal{R}_j$ with (distinct) constant deformation gradients in a compatible microstructure have deformation gradients that differ by a rank-one matrix [16] as in equation (1.1), which uniquely determines the direction of the normal to the interface in the deformed configuration. Therefore straight-line traces of interfaces are expected to separate such regions, which can be solved by the rank-one equation.

3. Assignment of martensite variants

In this section, we propose a mathematical method to assign a martensite variant to the specific region scanned by EBSD without knowing the orientation relationships.

Downloaded from https://royalsocietypublishing.org/ on 14 July 2022

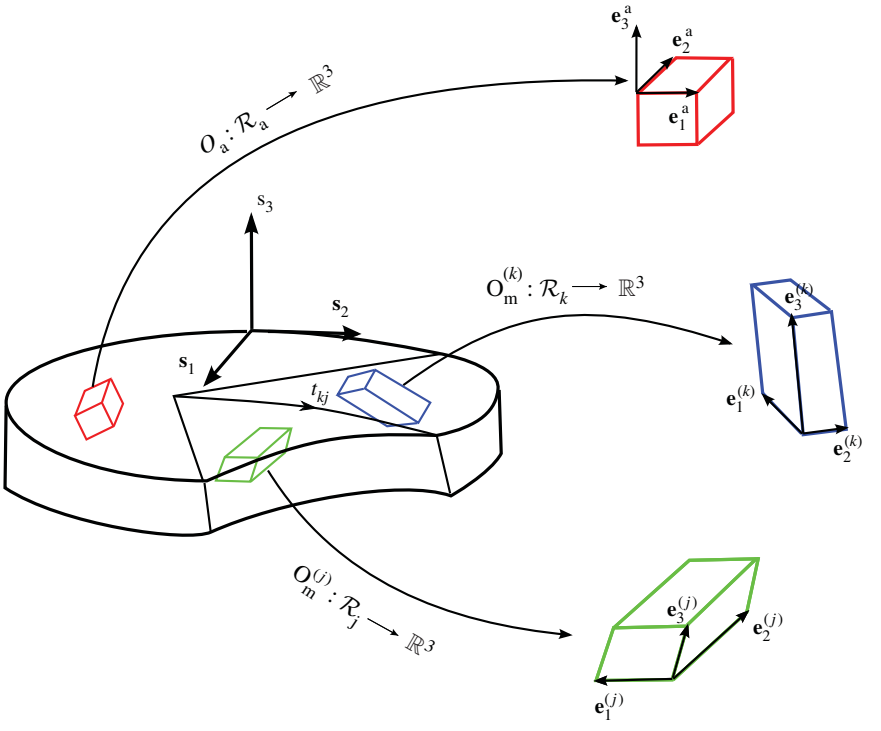

Figure 4. Schematic diagram of mappings from the machine base to the crystallographic base through the orientation matrices measured by EBSD. (Online version in colour.)

(a) Crystallography theory of martensite

For the phase transformation of $Cu_{25}Au_{30}Zn_{45}$ from cubic austenite to monoclinic martensite, the lattice bases can be expressed in matrix representations as $\mathbf{E}^a = (\mathbf{e}_1^a, \mathbf{e}_2^a, \mathbf{e}_3^a)$ and $\mathbf{E} = (\mathbf{e}_1, \mathbf{e}_2, \mathbf{e}_3)$ where $\mathbf{e}_i^a$ and $\mathbf{e}_i$ are calculated from the lattice parameters according to equation (A 2). Using the StrucTrans algorithm [40], the transformation stretch tensor $\mathbf{U}$ is determined corresponding to a lattice correspondence matrix $\boldsymbol{\Gamma} \in \mathbb{R}^{3\times3}$. Geometrically, the lattice correspondence matrix results in a set of sublattice vectors of austenite, $(\hat{\mathbf{e}}_1^a, \hat{\mathbf{e}}_2^a, \hat{\mathbf{e}}_3^a) = \mathbf{E}^a\boldsymbol{\Gamma}$ [41], which underlies a unit cell to be deformed to the primitive unit cell of martensite upon phase transformation. Thus, the set of vectors $(\mathbf{U}\hat{\mathbf{e}}_1^a, \mathbf{U}\hat{\mathbf{e}}_2^a, \mathbf{U}\hat{\mathbf{e}}_3^a)$ gives the lattice metric of the martensite unit cell, but their orientation may not match the observed martensite variant in the real microstructure.

The variants of martensite are symmetry-related according to the point groups of austenite and martensite. In particular, the point group of martensite should be a sub-group of austenite so that the solid–solid phase transformation is reversible [42]. Let $\mathcal{P} = \{\mathbf{Q}_1, \ldots, \mathbf{Q}_m\}$, $\mathbf{Q}_i \in \mathrm{O}(3)$ denote the point group of austenite; we define a set of symmetry-related martensite variants

$$\mathcal{U} = \{\mathbf{U}_1, \ldots, \mathbf{U}_n\} = \{\mathbf{Q}_i\mathbf{U}\mathbf{Q}_i^T : i = 1, \ldots, m\}. \tag{3.1}$$

Note that n can be less than m because one can have repetition. We choose $\mathbf{Q}_1 = \mathbf{I}$ so that $\mathbf{U}_1 = \mathbf{U}$.

In general, for a point group $\mathcal{P}$ of the Bravais lattice with primitive basis $\mathbf{P} = (\mathbf{p}_1, \mathbf{p}_2, \mathbf{p}_3)$, if $\mathbf{Q} \in \mathcal{P}$, there is a 3×3 matrix of integers $\mathbf{M} = M_{ij}$ with determinant ±1 such that

$$\mathbf{Q}\mathbf{p}_i = M_{ij}\mathbf{p}_j. \tag{3.2}$$

In matrix representation, we have $\mathbf{QP} = \mathbf{PM}$. All matrices determined by (3.2) for a Bravais lattice with lattice vectors $\mathbf{P}$ form a group, i.e. *a lattice group* [41–43]. The lattice group plays an important role in the determination of the lattice correspondence between austenite and

Downloaded from https://royalsocietypublishing.org/ on 14 July 2022

martensite upon structural transformation because the symmetry-related martensite variants result in the symmetry-related lattice correspondences [40].

The fundamental theorem of crystallography says that if $\mathbf{p}_1, \mathbf{p}_2, \mathbf{p}_3$ are primitive lattice vectors of a periodic structure, then all other possible primitive lattice vectors are given by $\tilde{\mathbf{p}}_i = \mu_i^j \mathbf{p}_j$, where the 3×3 matrix μ_i^j is a matrix of integers with determinant ± 1. The 3×3 matrices of integers with determinant ± 1 form a group, called GL(3, $\mathbb{Z}$). Among the 14 Bravais lattices, there are 7 complex lattices whose conventional lattice bases are not the same as the primitive bases. In the case that austenite belongs to one of those complex lattices, the relation between the conventional and primitive bases is calculated as $\mathbf{e}_i^a = \chi_i^j \mathbf{p}_j$ for the conversion matrix $\chi_i^j \in \mathbb{Z}^{3\times3}$. Using the indicial representation for the lattice correspondence given by the StrucTrans algorithm, the sublattice vectors $\hat{\mathbf{e}}_i^a = \gamma_i^j \mathbf{e}_j^a$ for a real matrix $\gamma_i^j \in \mathbb{R}^{3\times3}$, which can be expressed as $\hat{\mathbf{e}}_i^a = \bar{\gamma}_i^j \mathbf{p}_j$ for a matrix of integers $\bar{\gamma}_i^j = \gamma_i^k \chi_k^j$; the proof can be found in reference [41]. The associated transformation stretch tensor $\mathbf{U}$ deforms the sublattice cell of austenite to the primitive cell of martensite as

$$\gamma_k^i \mathbf{e}_k^a \cdot \mathbf{U}^2 \gamma_j^k \mathbf{e}_k^a = \mathbf{e}_i \cdot \mathbf{e}_j. \tag{3.3}$$

Using the matrix representation that $\gamma_i^j \mathbf{e}_j^a = \mathbf{E}^a \boldsymbol{\Gamma}$, equation (3.3) becomes

$$(\mathbf{E}^a \boldsymbol{\Gamma})^T \mathbf{U}^2 \mathbf{E}^a \boldsymbol{\Gamma} = \mathbf{E}^T \mathbf{E}. \tag{3.4}$$

By symmetry, there are n variants of martensite where n is the ratio of the order of the point group of austenite to that of the point group of martensite, i.e. $n = |\mathcal{P}|/|\mathcal{P}^m|$. For the cubic to monoclinic phase transformation, there are $n = 24/2 = 12$ variants of martensite. However, direct calculation of equation (3.1) results in $|\mathcal{P}|$ variants. This implies that going through every $\mathbf{Q}_\ell$ in $\mathcal{P}$ will result in some duplicate $\mathbf{U}_\ell$'s. Based on group theory, the multiplicity is equal to the order of the point group of martensite. For example, in the case of the cubic to monoclinic transformation, there exist two possible lattice correspondences mapping the different sublattices of austenite to the same primitive lattice of martensite. Let $\mathbf{M}^{a,m}$ be the lattice groups of austenite and martensite respectively, where $\mathbf{Q}_\ell \mathbf{P} = \mathbf{P}\mathbf{M}_\ell^a$ and $\mathbf{Q}_d^m \mathbf{E} = \mathbf{E}\mathbf{M}_d^m$ for $\mathbf{Q}_\ell \in \mathcal{P}$ and $\mathbf{Q}_d^m \in \mathcal{P}^m$. For any variant labelled by ℓ, Chen *et al*. [40] has proven a crystallographically equivalent form of (3.4)

$$(\mathbf{E}^a \boldsymbol{\Gamma}^{(\ell,d)})^T \mathbf{U}_\ell^2 \mathbf{E}^a \boldsymbol{\Gamma}^{(\ell,d)} = \mathbf{E}^T \mathbf{E} \tag{3.5}$$

where

$$\boldsymbol{\Gamma}^{(\ell,d)} = \mathbf{M}_\ell^a \boldsymbol{\Gamma} (\mathbf{M}_d^m)^{-1} \text{ and } \mathbf{U}_\ell = \mathbf{Q}_\ell \mathbf{U} \mathbf{Q}_\ell^T. \tag{3.6}$$

The double-superscript matrix $\boldsymbol{\Gamma}^{(\ell,d)}$ represents the lattice correspondence congruous with the variant $\mathbf{U}_\ell$. The superscript ℓ denotes the indices giving unique variants, where $\ell \in \{1, 2, \ldots, |\mathcal{P}|/|\mathcal{P}^m|\}$. The superscript d represents the multiplicity of the variant ℓ where $d = 1, \ldots, |\mathcal{P}^m|$. Applying (3.1) and (3.6), all variants and their congruous lattice correspondence can be computed in terms of the cubic basis of the crystal.

The above equation can be also expressed in the machine basis through the orientation matrix characterized by EBSD. From the orientation matrix of austenite $\mathbf{O}_a = \mathbf{G}_a \mathbf{E}^a$ where $\mathbf{G}_a$ is calculated by (A 4) from three Euler angles $(\varphi_1^a, \Phi^a, \varphi_2^a)$, the left-hand side of equation (3.5) can be written as,

$$\text{l.h.s} = (\mathbf{O}_a \boldsymbol{\Gamma}^{(\ell,d)})^T [\mathbf{C}_\ell]_a \mathbf{O}_a \boldsymbol{\Gamma}^{(\ell,d)}. \tag{3.7}$$

The term $[\mathbf{C}_\ell]_a = \mathbf{G}_a \mathbf{U}_\ell^2 \mathbf{G}_a^T$ underlies the components of the Right Cauchy–Green tensor in terms of the machine basis for the stretch tensor $\mathbf{U}_\ell$. The right-hand side of equation (3.5) is invariant of rotation, thus

$$(\mathbf{O}_a \boldsymbol{\Gamma}^{(\ell,d)})^T [\mathbf{C}_\ell]_a \mathbf{O}_a \boldsymbol{\Gamma}^{(\ell,d)} = \mathbf{E}^T \mathbf{E}. \tag{3.8}$$

For a given material that transforms from the point group $\mathcal{P}$ to the point group $\mathcal{P}^m$ with $\mathcal{P}^m \subset \mathcal{P}$, any pair $(\mathbf{U}_\ell, \boldsymbol{\Gamma}^{(\ell,d)})$ where $\ell = 1, \ldots, |\mathcal{P}|$, $d = 1, \ldots, |\mathcal{P}^m|$ should satisfy the equality (3.8) up to experimental errors. For a specific domain in austenite corresponding to the sub-region

Downloaded from https://royalsocietypublishing.org/ on 14 July 2022

in martensite characterized by the orientation matrix $\mathbf{O}_m = \mathbf{G}_m\mathbf{E}$, there exists a sufficiently small rotation $\mathbf{R} \in SO(3)$ such that

$$\mathbf{R}\mathbf{U}_{\ell^\star}\mathbf{O}_a\boldsymbol{\Gamma}^{(\ell^\star,d^\star)} = \mathbf{O}_m \text{ for some } \ell^\star \in \{1,\ldots,|\mathcal{P}|/|\mathcal{P}^m|\}, d^\star \in \{1,\ldots,|\mathcal{P}^m|\}. \tag{3.9}$$

This equation is true because of the rigidity of the solid–solid transformation [44]. Although the EBSD experiment does not provide direct orientation parallelisms of crystallographic planes and directions between the austenite and martensite lattices, equation (3.9) indicates that the assignment of a variant to a certain sub-region in martensite is subjected to finite options in the order of the point group of austenite.

(b) Method of variant assignment

In this section, we propose a procedure to assign variants to the sub-regions of martensite characterized by EBSD. Within each of the regions, the Euler angles are measured and converted to the orientation matrices for austenite $\mathbf{O}_a$ and martensite $\mathbf{O}_m^{(k)}$ for $k \in \{1,2,\ldots,N\}$. From the X-ray diffraction characterization and the StrucTrans algorithm, we obtain the transformation stretch tensor $\mathbf{U}$ and its corresponding $\boldsymbol{\Gamma}$, which are labelled as $\mathbf{U}_1$ and $\boldsymbol{\Gamma}^{(1,1)}$. The following procedure outlines how to assign the deformation to a specific region of martensite:

(i) Examine whether the conventional lattice basis of austenite is the same as its primitive basis. If yes, proceed to the next step. If not, derive the conversion matrix $\boldsymbol{\chi}$ by

$$\boldsymbol{\chi} = \mathbf{P}^{-1}\mathbf{E}^a, \tag{3.10}$$

where the primitive basis is $\mathbf{P} = (\mathbf{p}_1, \mathbf{p}_2, \mathbf{p}_3)$ and conventional basis is $\mathbf{E}^a = (\mathbf{e}_1^a, \mathbf{e}_2^a, \mathbf{e}_3^a)$. Label $\boldsymbol{\chi}\boldsymbol{\Gamma}^{(1,1)}$ to be the new $\boldsymbol{\Gamma}^{(1,1)}$. If the conventional lattice basis of martensite is not the same as its primitive basis, label $\boldsymbol{\Gamma}^{(1,1)}\boldsymbol{\chi}^{-1}$ to be the new $\boldsymbol{\Gamma}^{(1,1)}$ where $\boldsymbol{\chi}$ is the conversion matrix derived in the same way as in (3.10).

(ii) Determine $n = |\mathcal{P}|/|\mathcal{P}^m|$ distinct martensite variants where $\mathcal{P}$ and $\mathcal{P}^m$ are the point groups of austenite and martensite with $\mathcal{P}^m \subset \mathcal{P}$.
First, generate a set of martensite variants

$$\mathcal{M} = \{(\mathbf{U}_i, \mathbf{Q}_i, \mathbf{M}_i) : \mathbf{U}_i = \mathbf{Q}_i\mathbf{U}_1\mathbf{Q}_i^T \text{ and } \mathbf{M}_i = \mathbf{P}^{-1}\mathbf{Q}_\ell\mathbf{P} \text{ for } \mathbf{Q}_i \in \mathcal{P}\}. \tag{3.11}$$

The set $\mathcal{M}$ can be divided into n subsets containing the elements with the same $\mathbf{U}_i$ [3,41,42]; that is $\mathcal{M} = \mathcal{A}_1 \cup \ldots \cup \mathcal{A}_n$ where $n = |\mathcal{P}|/|\mathcal{P}^m|$. Each of the subsets

$$\mathcal{A}_\ell = \{(\mathbf{U}_\ell, \mathbf{Q}_{(\ell,d)}, \mathbf{M}_{(\ell,d)}) \text{ for } d = 1,\ldots,|\mathcal{P}^m|\}, \tag{3.12}$$

represents a distinct variant of martensite.

(iii) For each of the subsets $\mathcal{A}_\ell$, calculate the lattice correspondence matrices

$$\boldsymbol{\Gamma}^{(\ell,d)} = \mathbf{M}_{(\ell,d)}\boldsymbol{\Gamma}^{(1,1)}, \text{ for } d = 1,\ldots,|\mathcal{P}^m|. \tag{3.13}$$

Note that the above calculation is equivalent to (3.6) due to the group-subgroup relation between austenite and martensite [41]. All lattice correspondence matrices form a set

$$\mathcal{V} = \{(\mathbf{C}_\ell, \boldsymbol{\Gamma}^{(\ell,d)}) : \ell = 1,\ldots,|\mathcal{P}|/|\mathcal{P}^m|, d = 1,\ldots,|\mathcal{P}^m|\}, \tag{3.14}$$

where the Right Cauchy Green tensor is given by:

$$\mathbf{C}^{(\ell,d)} = (\mathbf{O}_a\boldsymbol{\Gamma}^{(\ell,d)})^{-\mathrm{T}}\mathbf{E}^{\mathrm{T}}\mathbf{E}(\mathbf{O}_a\boldsymbol{\Gamma}^{(\ell,d)})^{-1}. \tag{3.15}$$

(iv) In a specific martensite sub-region $\mathcal{R}_k$ corresponding to orientation matrix $\mathbf{O}_m^{(k)}$, calculate the set of rotations

$$\mathcal{S}_k = \{\mathbf{R}^{(\ell,d)} : \mathbf{R}^{(\ell,d)} = \mathbf{O}_m^{(k)}(\sqrt{\mathbf{C}^{(\ell,d)}}\mathbf{O}_a\boldsymbol{\Gamma}^{(\ell,d)})^{-1} \text{ for all } (\mathbf{C}_\ell, \boldsymbol{\Gamma}^{(\ell,d)}) \in \mathcal{V}\}. \tag{3.16}$$

Given the fact that the relative rotation of the lattice of the martensite to that of austenite is near to the identity matrix [44], a pair of labels $(\ell^\star, d^\star) \in \{1,\ldots,|\mathcal{P}|/|\mathcal{P}^m|\} \times \{1,\ldots,|\mathcal{P}^m|\}$

Downloaded from https://royalsocietypublishing.org/ on 14 July 2022

minimizes the distance

$$\text{dist} = \|\mathbf{R}^{(\ell,d)} - \mathbf{I}\|, \text{ for all } \ell = 1, \ldots, |\mathcal{P}|/|\mathcal{P}^m|, \ d = 1, \ldots, |\mathcal{P}^m|. \tag{3.17}$$

The symbol $\|\cdot\|$ denotes the L2 norm of a matrix. In this representation, we use the angle of rotation

$$\cos\theta^{(\ell,d)} = \frac{\text{tr}\mathbf{R}^{(\ell,d)} - 1}{2}, \tag{3.18}$$

as the measure of rotations.

In the case of the cubic to monoclinic phase transformation in $Cu_{25}Au_{30}Zn_{45}$ alloy, we have

$$\mathbf{E}^a = (\mathbf{e}_1^a, \mathbf{e}_2^a, \mathbf{e}_3^a) = a_0\mathbf{I}, \quad \mathbf{E} = (\mathbf{e}_1, \mathbf{e}_2, \mathbf{e}_3) = \begin{pmatrix} a\sin\beta & 0 & 0 \\ 0 & b & 0 \\ a\cos\beta & 0 & c \end{pmatrix}. \tag{3.19}$$

Equation (3.5) shows that the transformation stretch tensor $\mathbf{U}_1$ is calculated as the polar decomposition of $\mathbf{E}(\mathbf{E}^a\boldsymbol{\Gamma}^{(1,d)})^{-1}$ with $d = 1, 2$ where

$$\boldsymbol{\Gamma}^{(1,1)} = \begin{pmatrix} -\frac{1}{2} & 0 & \frac{m}{2} \\ 0 & 1 & 0 \\ -\frac{1}{2} & 0 & -\frac{m}{2} \end{pmatrix} \quad \text{and} \quad \boldsymbol{\Gamma}^{(1,2)} = \begin{pmatrix} \frac{1}{2} & 0 & -\frac{m}{2} \\ 0 & 1 & 0 \\ \frac{1}{2} & 0 & \frac{m}{2} \end{pmatrix}. \tag{3.20}$$

In (3.20), $m = 9$ is an integer that denotes the modulation for long period stacking order structure of martensite [34]. We can explicitly write the Right Cauchy–Green tensor for $\mathbf{U}_1$ as

$$\mathbf{C}_1 = \mathbf{U}_1^2 = \begin{pmatrix} \frac{c^2 + a^2m^2 + 2acm\cos\beta}{a_0^2m^2} & 0 & \frac{c^2 - a^2m^2}{a_0^2m^2} \\ 0 & \frac{b^2}{a_0^2} & 0 \\ \frac{c^2 - a^2m^2}{a_0^2m^2} & 0 & \frac{c^2 + a^2m^2 - 2acm\cos\beta}{a_0^2m^2} \end{pmatrix}. \tag{3.21}$$

Equation (3.21) implies that the components of $\mathbf{U}_1$ only depend on the lattice parameters of austenite and martensite which were determined by X-ray measurement; the components are $\alpha = 1.0591$, $\epsilon = 0.0073$, $\delta = 1.0015$, $\gamma = 0.9363$ and $m = 9$. Table 3 lists all the correlated martensite variant pairs of $(\mathbf{U}_\ell, \boldsymbol{\Gamma}^{(\ell,d)})$ calculated from (3.11) and (3.12) in step (ii) of the variant assignment algorithm.

The martensite domains are distinguishable in the orientation map of figure 2. The Euler angles for the austenite and sub-regions of martensite $\mathcal{R}_1$, $\mathcal{R}_2$, $\mathcal{R}_3$, $\mathcal{R}_4$ are listed in table 4. Following the steps (iii) and (iv) of the variant assignment algorithm, we calculate the set of rotations S_k for each of the sub-regions $\mathcal{R}_k$, $k = 1, 2, 3, 4$, expressed as the angle of rotations $\theta^{(\ell,d)}$ calculated by (3.18) in table 5. It is clear that there is only one angle of rotation much smaller than all other angles in each of the martensite sub-regions. Note that the angle of rotation underlies the orientation relationship between martensite and austenite. For a non-diffusive phase transformation in solids, the elastic rigidity restricts the rotation between the product phase and the parent phase. Therefore, the sub-region is assigned to be the martensite variant corresponding to the smallest angle of rotation relative to austenite. The deformation gradient in each of the assigned martensite regions is calculated by

$$\mathbf{F}_k(\ell^\star, d^\star) = \mathbf{O}_m^{(k)}(\mathbf{O}_a\boldsymbol{\Gamma}^{(\ell^\star,d^\star)})^{-1} \quad \text{for } k = 1, 2, 3, 4. \tag{3.22}$$

Downloaded from https://royalsocietypublishing.org/ on 14 July 2022

Table 3. Martensite variants and the associated lattice correspondences. The over lines of the entries denote the negative sign.

	variant	Γ			variant	Γ	
ℓ	$\mathbf{U}_\ell$	$(\ell,1)$	$(\ell,2)$	ℓ	$\mathbf{U}_\ell$	$(\ell,1)$	$(\ell,2)$
1	$\begin{bmatrix} \alpha & 0 & -\epsilon \\ 0 & \gamma & 0 \\ -\epsilon & 0 & \delta \end{bmatrix}$	$\begin{bmatrix} \frac{-1}{2} & 0 & \frac{m}{2} \\ 0 & 1 & 0 \\ \frac{-1}{2} & 0 & \frac{-m}{2} \end{bmatrix}$	$\begin{bmatrix} \frac{1}{2} & 0 & \frac{-m}{2} \\ 0 & 1 & 0 \\ \frac{1}{2} & 0 & \frac{m}{2} \end{bmatrix}$	7	$\begin{bmatrix} \alpha & -\epsilon & 0 \\ -\epsilon & \delta & 0 \\ 0 & 0 & \gamma \end{bmatrix}$	$\begin{bmatrix} \frac{1}{2} & 0 & \frac{-m}{2} \\ \frac{1}{2} & 0 & \frac{m}{2} \\ 0 & -1 & 0 \end{bmatrix}$	$\begin{bmatrix} \frac{-1}{2} & 0 & \frac{m}{2} \\ \frac{-1}{2} & 0 & \frac{-m}{2} \\ 0 & -1 & 0 \end{bmatrix}$
2	$\begin{bmatrix} \alpha & 0 & \epsilon \\ 0 & \gamma & 0 \\ \epsilon & 0 & \delta \end{bmatrix}$	$\begin{bmatrix} \frac{-1}{2} & 0 & \frac{m}{2} \\ 0 & -1 & 0 \\ \frac{1}{2} & 0 & \frac{m}{2} \end{bmatrix}$	$\begin{bmatrix} \frac{1}{2} & 0 & \frac{-m}{2} \\ 0 & -1 & 0 \\ \frac{-1}{2} & 0 & \frac{-m}{2} \end{bmatrix}$	8	$\begin{bmatrix} \delta & 0 & \epsilon \\ 0 & \gamma & 0 \\ \epsilon & 0 & \alpha \end{bmatrix}$	$\begin{bmatrix} \frac{-1}{2} & 0 & \frac{-m}{2} \\ 0 & 1 & 0 \\ \frac{1}{2} & 0 & \frac{-m}{2} \end{bmatrix}$	$\begin{bmatrix} \frac{1}{2} & 0 & \frac{m}{2} \\ 0 & 1 & 0 \\ \frac{-1}{2} & 0 & \frac{m}{2} \end{bmatrix}$
3	$\begin{bmatrix} \gamma & 0 & 0 \\ 0 & \alpha & \epsilon \\ 0 & \epsilon & \delta \end{bmatrix}$	$\begin{bmatrix} 0 & 1 & 0 \\ \frac{-1}{2} & 0 & \frac{m}{2} \\ \frac{1}{2} & 0 & \frac{m}{2} \end{bmatrix}$	$\begin{bmatrix} 0 & 1 & 0 \\ \frac{1}{2} & 0 & \frac{-m}{2} \\ \frac{-1}{2} & 0 & \frac{-m}{2} \end{bmatrix}$	9	$\begin{bmatrix} \gamma & 0 & 0 \\ 0 & \delta & -\epsilon \\ 0 & -\epsilon & \alpha \end{bmatrix}$	$\begin{bmatrix} 0 & 1 & 0 \\ \frac{-1}{2} & 0 & \frac{-m}{2} \\ \frac{-1}{2} & 0 & \frac{m}{2} \end{bmatrix}$	$\begin{bmatrix} 0 & 1 & 0 \\ \frac{1}{2} & 0 & \frac{m}{2} \\ \frac{1}{2} & 0 & \frac{-m}{2} \end{bmatrix}$
4	$\begin{bmatrix} \gamma & 0 & 0 \\ 0 & \alpha & -\epsilon \\ 0 & -\epsilon & \delta \end{bmatrix}$	$\begin{bmatrix} 0 & -1 & 0 \\ \frac{1}{2} & 0 & \frac{-m}{2} \\ \frac{1}{2} & 0 & \frac{m}{2} \end{bmatrix}$	$\begin{bmatrix} 0 & -1 & 0 \\ \frac{-1}{2} & 0 & \frac{m}{2} \\ \frac{-1}{2} & 0 & \frac{-m}{2} \end{bmatrix}$	10	$\begin{bmatrix} \delta & -\epsilon & 0 \\ -\epsilon & \alpha & 0 \\ 0 & 0 & \gamma \end{bmatrix}$	$\begin{bmatrix} \frac{-1}{2} & 0 & \frac{-m}{2} \\ \frac{-1}{2} & 0 & \frac{m}{2} \\ 0 & 1 & 0 \end{bmatrix}$	$\begin{bmatrix} \frac{1}{2} & 0 & \frac{m}{2} \\ \frac{1}{2} & 0 & \frac{-m}{2} \\ 0 & 1 & 0 \end{bmatrix}$
5	$\begin{bmatrix} \delta & 0 & -\epsilon \\ 0 & \gamma & 0 \\ -\epsilon & 0 & \alpha \end{bmatrix}$	$\begin{bmatrix} \frac{-1}{2} & 0 & \frac{-m}{2} \\ 0 & -1 & 0 \\ \frac{-1}{2} & 0 & \frac{m}{2} \end{bmatrix}$	$\begin{bmatrix} \frac{1}{2} & 0 & \frac{m}{2} \\ 0 & -1 & 0 \\ \frac{1}{2} & 0 & \frac{-m}{2} \end{bmatrix}$	11	$\begin{bmatrix} \gamma & 0 & 0 \\ 0 & \delta & \epsilon \\ 0 & \epsilon & \alpha \end{bmatrix}$	$\begin{bmatrix} 0 & \bar{1} & 0 \\ \frac{-1}{2} & 0 & \frac{-m}{2} \\ \frac{1}{2} & 0 & \frac{-m}{2} \end{bmatrix}$	$\begin{bmatrix} 0 & -1 & 0 \\ \frac{1}{2} & 0 & \frac{m}{2} \\ \frac{-1}{2} & 0 & \frac{m}{2} \end{bmatrix}$
6	$\begin{bmatrix} \alpha & \epsilon & 0 \\ \epsilon & \delta & 0 \\ 0 & 0 & \gamma \end{bmatrix}$	$\begin{bmatrix} \frac{1}{2} & 0 & \frac{-m}{2} \\ \frac{-1}{2} & 0 & \frac{-m}{2} \\ 0 & 1 & 0 \end{bmatrix}$	$\begin{bmatrix} \frac{-1}{2} & 0 & \frac{m}{2} \\ \frac{1}{2} & 0 & \frac{m}{2} \\ 0 & 1 & 0 \end{bmatrix}$	12	$\begin{bmatrix} \delta & \epsilon & 0 \\ \epsilon & \alpha & 0 \\ 0 & 0 & \gamma \end{bmatrix}$	$\begin{bmatrix} \frac{1}{2} & 0 & \frac{m}{2} \\ \frac{-1}{2} & 0 & \frac{m}{2} \\ 0 & -1 & 0 \end{bmatrix}$	$\begin{bmatrix} \frac{-1}{2} & 0 & \frac{-m}{2} \\ \frac{1}{2} & 0 & \frac{-m}{2} \\ 0 & -1 & 0 \end{bmatrix}$

royalsocietypublishing.org/journal/rsta *Phil. Trans. R. Soc. A* **379**: 20200112

Downloaded from https://royalsocietypublishing.org/ on 14 July 2022

Table 4. The Euler angles mapping the crystal base to the machine base measured from EBSD for the austenite (figure 2) and four regions of martensite (figure 3). The orientation matrix follows the 3-1-3 rotation sequence.

region		ϕ_1	Ψ	ϕ_2	variant
austenite		134.4	12.4	16	**I**
martensite	$\mathcal{R}_1$	11	81.1	172.6	$\mathbf{U}_6$
	$\mathcal{R}_2$	159.1	141.1	103.9	$\mathbf{U}_9$
	$\mathcal{R}_3$	110.9	101.1	352.4	$\mathbf{U}_7$
	$\mathcal{R}_4$	145.9	62.6	278.9	$\mathbf{U}_{11}$

Table 5. The angles $\theta^{(\ell,d)}$ for the martensite regions $\mathcal{R}_k$, $k = 1, 2, 3, 4$.

	$\mathcal{R}_1$		$\mathcal{R}_2$		$\mathcal{R}_3$		$\mathcal{R}_4$	
$\theta(^\circ)$	d		d		d		d	
ℓ	1	2	1	2	1	2	1	2
1	172.63	90.83	120.36	118.85	173.11	91.87	117.96	121.02
2	177.56	89.69	113.58	127.74	176.19	88.67	127.26	114.23
3	122.46	113.70	83.34	96.93	117.97	124.80	176.10	177.76
4	118.48	125.76	176.84	175.39	124.16	113.50	97.07	83.11
5	121.81	117.82	171.30	91.35	122.33	116.08	91.47	171.99
6	**7.79**	173.06	174.47	84.72	178.39	177.83	175.89	94.56
7	179.43	176.52	95.70	175.92	**8.04**	172.43	85.88	174.23
8	126.40	114.38	89.31	179.08	126.61	115.42	178.14	89.12
9	86.73	174.69	173.20	**8.81**	175.79	92.43	178.82	175.65
10	96.99	83.12	112.35	121.53	177.33	179.60	119.33	125.95
11	93.69	175.50	178.98	174.50	173.51	88.09	173.01	**8.31**
12	177.94	177.13	120.03	126.60	82.47	97.60	112.82	122.36

For the four regions characterized in figure 3*b*, the $(\ell^\star, d^\star)$ pairs are $(6, 1)$, $(9, 2)$, $(7, 1)$ and $(11, 2)$, respectively. The assignment of variant to each of the sub-regions is summarized as

$$\mathcal{R}_1 \to \mathbf{U}_6,\ \mathcal{R}_2 \to \mathbf{U}_9,\ \mathcal{R}_3 \to \mathbf{U}_7,\ \mathcal{R}_4 \to \mathbf{U}_{11}. \tag{3.23}$$

The deformation gradients in each of the martensite sub-regions can be expressed in machine basis as

$$\mathbf{F}_1 = \begin{bmatrix} 1.0015 & -0.1323 & -0.0845 \\ 0.0877 & 1.0388 & -0.0219 \\ 0.0630 & 0.0553 & 0.9379 \end{bmatrix}, \quad \mathbf{F}_2 = \begin{bmatrix} 0.9659 & -0.0965 & 0.0106 \\ -0.0092 & 1.014 & 0.1642 \\ -0.0207 & -0.1296 & 0.9934 \end{bmatrix}$$

and

$$\mathbf{F}_3 = \begin{bmatrix} 1.0059 & 0.1176 & -0.0014 \\ -0.1657 & 1.0287 & 0.0006 \\ -0.0021 & 0.0042 & 0.9422 \end{bmatrix}, \ \mathbf{F}_4 = \begin{bmatrix} 0.9582 & -0.0356 & 0.1289 \\ -0.0601 & 1.0268 & -0.0605 \\ -0.127 & 0.0799 & 0.9906 \end{bmatrix}.$$

We use the assigned variants in sub-regions $\mathcal{R}_i$, $i = 1, 2, 3, 4$ to study their twinning relations by solving the crystallographic equations of martensite [3]. We find that $\mathcal{R}_1$ and $\mathcal{R}_2$ forms Type-I/II twins about the twofold axis [101] written in cubic basis of austenite. The same calculations for other neighbouring sub-regions yield that $\mathcal{R}_1$ and $\mathcal{R}_3$ forms Compound twins about two twofold

Downloaded from https://royalsocietypublishing.org/ on 14 July 2022

Table 6. Measure of rank-one ability between any of neighbouring martensite sub-regions.

sub-regions	$(\mathcal{R}_1, \mathcal{R}_2)$	$(\mathcal{R}_1, \mathcal{R}_3)$	$(\mathcal{R}_1, \mathcal{R}_4)$	$(\mathcal{R}_2, \mathcal{R}_3)$	$(\mathcal{R}_2, \mathcal{R}_4)$	$(\mathcal{R}_3, \mathcal{R}_4)$
$\mathcal{C}_{(k1,k2)}$	0.04543	0.06960	0.05788	0.06409	0.06300	0.03444

Table 7. Measure of rank-one ability between any of neighbouring martensite sub-regions.

sub-region	$\mathcal{R}_1$	$\mathcal{R}_2$	$\mathcal{R}_3$	$\mathcal{R}_4$
$\|\mathrm{cof}(\mathbf{F}_k - \mathbf{I})\|$	0.02273	0.02759	0.02395	0.02516

axes [100] and [010]; $\mathcal{R}_1$ and $\mathcal{R}_4$ forms Type-I/II twins about the twofold axis $[10\bar{1}]$; $\mathcal{R}_2$ and $\mathcal{R}_3$ forms Type-I/II twins about twofold axis $[10\bar{1}]$; $\mathcal{R}_2$ and $\mathcal{R}_4$ forms Compound twins about two twofold axes [001] and [010]; $\mathcal{R}_3$ and $\mathcal{R}_4$ forms Type-I/II twins about the twofold axis [101]. The cofactor conditions for this specific microstructure are $(\mathrm{CC})_2 = 1.03385$ for [101] Type-I twin, $(\mathrm{CC})_2 = 0.96950$ for [101] Type-II twin, and $(\mathrm{CC})_2 = 0$ for Compound twin.

4. Rank-one connections and compatibility

The rank-one connections between the deformation gradients $\mathbf{F}_{k1}$, $\mathbf{F}_{k2}$ in neighbouring regions are examined as the cofactor of $(\mathbf{F}_{k1} - \mathbf{F}_{k2})$. The cofactor of a matrix $\mathbf{A} \in \mathbb{R}^{p\times p}$ can be calculated as

$$\mathrm{cof}(\mathbf{A})_{i,j} = (-1)^{i+j} \det(M_{ij}) \text{ for all } i, j \in \{1, 2, \ldots, p\} \tag{4.1}$$

where the matrix minors $M_{ij} \in \mathbb{R}^{(p-1)\times(p-1)}$ are computed by removing the ith row and the jth column of $\mathbf{A}$. Then we define

$$\mathcal{C}_{(k1,k2)} = \|\mathrm{cof}(\mathbf{F}_{k1} - \mathbf{F}_{k2})\| \tag{4.2}$$

as the measure of the rank-one ability between two deformation gradients $\mathbf{F}_{k1}$ and $\mathbf{F}_{k2}$. For the sub-regions $\mathcal{R}_1, \mathcal{R}_2, \mathcal{R}_3$ and $\mathcal{R}_4$ in martensite in figure 2*d*, we calculate the expression (4.2) between any two of the assigned martensite variants, the results are shown in table 6. Similarly, we can check the rank-one ability between each of the martensite sub-regions and austenite by $\|\mathrm{cof}(\mathbf{F}_k - \mathbf{I})\|$, as examined in table 7.

The kinematics of (4.2) suggests that it underlies a measure of the areal compatibility of an interface deformed by $\mathbf{F}_{k1}$ and $\mathbf{F}_{k2}$, respectively, from different sides. This quantity is related to the out-of-plane discrepancies caused by incompatibility between the neighbouring deformation gradients. Note that it cannot be understood as the elastic strain. For a specific twin system with twinning plane normal $\mathbf{n}_0$, the magnitude of $\mathrm{cof}(\mathbf{F}_{k1} - \mathbf{F}_{k2})\mathbf{n}_0$ calculates the area difference at the interface between neighbouring martensite variants. For this special alloy whose lattice parameters closely satisfy all sub-conditions of cofactor conditions [34], the interface mismatch between a single variant of martensite and austenite is even smaller than that of a twinning interface. As shown in figure 1*b*, very coarse laths with sub-millimetre width can grow from the austenite upon structural transformation. This is unusual for a martensite material undergoing the first-order phase transformation with such a large volume change. The quantitative measures of compatibility of microstructures are super critical to the mechanical property of shape memory alloys. Our approach provides a way to quantitatively analyse the martensite/martensite and austenite/martensite interfaces and their elastic compatibility.

5. Conclusion

Diffraction-based probes are useful characterization tools to study the formation of microstructure for phase-transforming materials. This paper proposes a mathematical model for the quantitative analysis of compatible interfaces of martensite by EBSD without assuming the crystallographic orientation relationships from the parent phase. The algorithm is implemented for cubic to

Downloaded from https://royalsocietypublishing.org/ on 14 July 2022

long atomic layer modulated monoclinic transformation of the alloy, $CuAu_{30}Zn_{45}$. Through the calculation of relative areal mismatch between neighbouring variants, the rational comparison of the rank-one ability can be conducted among different types of interfaces. When such quantitative analysis is combined with the thermal and mechanical characterizations, the structure–property relationship of the studied material can be established for further development.

Data accessibility. This article has no additional data.

Competing interests. We declare we have no competing interests.

Funding. This work was supported by: EPSRC grant no. EP/R014604/1 and RGC grant nos. 16201019 and 16207017 and CRF grant no. C6016-20G-C.

Acknowledgements. X.C., M.C., M.D.G. and R.D.J. acknowledge the financial support of MURI Project No. FA9550-12-1-0458 (administered by AFOSR). X.C. acknowledges the financial support of the HK Research Grants Council under grant nos. 16201019 and 16207017 and CRF grant no. C6016-20G-C. The authors X.C. and R.D.J. would like to thank the Isaac Newton Institute for Mathematical Sciences for support and hospitality during the programme: DNM The mathematical design of new materials. R.D.J. and M.D.G. have also benefited from the support of a Vannevar Bush Faculty Fellowship.

Appendix A. From Euler angles to conventional lattice vectors

In this appendix, we show explicitly how to obtain the conventional lattice basis of a Bravais lattice from the three Euler angles φ_1, Φ and φ_2 measured by EBSD. Let $\mathbf{e}_i$ $i,=1,2,3$ be the [100], [010] and [001] directions of a conventional unit cell, respectively. We can choose a rectangular Cartesian coordinate system (i.e. the cubic basis of crystal), $\hat{i}-\hat{j}-\hat{k}$, attached to the lattice origin, so that $\mathbf{e}_i$ can be expressed explicitly with respect to the cubic basis $\hat{i}-\hat{j}-\hat{k}$ as shown in figure 5. As a standard convention, the lattice parameters $a, b, c, \alpha, \beta, \gamma$ satisfy

$$\left.\begin{aligned} &|\mathbf{e}_1| = a, \quad |\mathbf{e}_2| = b, \quad |\mathbf{e}_3| = c, \\ \text{and} \quad &\mathbf{e}_1 \cdot \mathbf{e}_2 = ab\cos\gamma, \quad \mathbf{e}_2 \cdot \mathbf{e}_3 = bc\cos\alpha, \quad \mathbf{e}_3 \cdot \mathbf{e}_1 = ac\cos\beta, \end{aligned}\right\} \tag{A 1}$$

and $(\mathbf{e}_1 \times \mathbf{e}_2) \cdot \mathbf{e}_3 > 0$. The alignment between cubic basis $\hat{i}-\hat{j}-\hat{k}$ and lattice basis follows the rules:

(i) $\hat{k} \parallel \mathbf{e}_3$,
(ii) $\hat{i} \perp \mathbf{e}_2$ and $\hat{i} \perp \mathbf{e}_3$. So, $\hat{i} \parallel \mathbf{e}_3 \times \mathbf{e}_2$.
(iii) $\hat{j} = \hat{k} \times \hat{i}$.

In the cubic basis $\hat{i}-\hat{j}-\hat{k}$, the conventional lattice basis of a Bravais lattice can be written explicitly as

$$\left.\begin{aligned} \mathbf{e}_1 &= a\sqrt{\sin^2\beta - \frac{(\cos\gamma - \cos\alpha\cos\beta)^2}{\sin^2\alpha}}\hat{i} + a\frac{\cos\gamma - \cos\alpha\cos\beta}{\sin\alpha}\hat{j} + a\cos\beta\hat{k} \\ \mathbf{e}_2 &= b\sin\alpha\hat{j} + b\cos\alpha\hat{k} \\ \text{and} \quad \mathbf{e}_3 &= c\hat{k} \end{aligned}\right\} \tag{A 2}$$

For example, for a monoclinic lattice, $\alpha = \gamma = 90^\circ \neq \beta$, we have $\mathbf{e}_1 = a\sin\beta\hat{i} + a\cos\beta\hat{k}$. In matrix representation, the monoclinic basis is

$$(\mathbf{e}_1, \mathbf{e}_2, \mathbf{e}_3) = \begin{bmatrix} a\sin\beta & 0 & 0 \\ 0 & b & 0 \\ a\cos\beta & 0 & c \end{bmatrix}. \tag{A 3}$$

By EBSD measurement, we obtain three Euler angles φ_1, Φ and φ_2 relating $\hat{i}-\hat{j}-\hat{k}$ to the machine basis $\mathbf{s}_i$. In our experiment, the Euler angles correspond to a $\hat{k}-\hat{i}-\hat{k}$ rotation sequence.

Downloaded from https://royalsocietypublishing.org/ on 14 July 2022

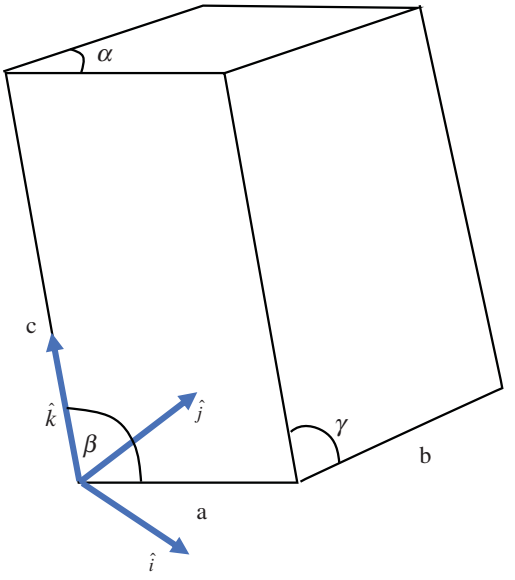

Figure 5. Convention of lattice basis with respect to the cubic basis $\hat{i} - \hat{j} - \hat{k}$. (Online version in colour.)

As a result, the rotation matrix is calculated as

$$\mathbf{G} = \mathbf{G}(\varphi_1, \Phi, \varphi_2) = \mathbf{G}_{\varphi_2}\mathbf{G}_{\Phi}\mathbf{G}_{\varphi_1}, \tag{A 4}$$

where

$$\mathbf{G}_{\varphi_1} = \begin{pmatrix} \cos\varphi_1 & \sin\varphi_1 & 0 \\ -\sin\varphi_1 & \cos\varphi_1 & 0 \\ 0 & 0 & 1 \end{pmatrix},$$

$$\mathbf{G}_{\Phi} = \begin{pmatrix} 1 & 0 & 0 \\ 0 & \cos\Phi & \sin\Phi \\ 0 & -\sin\Phi & \cos\Phi \end{pmatrix},$$

and

$$\mathbf{G}_{\varphi_2} = \begin{pmatrix} \cos\varphi_2 & \sin\varphi_2 & 0 \\ -\sin\varphi_2 & \cos\varphi_2 & 0 \\ 0 & 0 & 1 \end{pmatrix}.$$

Combining the equation (A 2), we have

$$\mathbf{O} = \mathbf{G}(\mathbf{e}_1, \mathbf{e}_2, \mathbf{e}_3). \tag{A 5}$$

References

1. Bowden PB, Young RJ. 1974 Deformation mechanisms in crystalline polymers. *J. Mater. Sci.* **9**, 2034–2051. (doi:10.1007/BF00540553)
2. Otsuka K, Wayman CM. 1999 *Shape memory materials*. Cambridge, UK: Cambridge University Press.
3. Bhattacharya K 2003 *Microstructure of martensite: why it forms and how it gives rise to the shape-memory effect*, vol. 2. Oxford series on materials modeling. Oxford, UK: Oxford University Press.
4. Meng H, Li G. 2013 A review of stimuli-responsive shape memory polymer composites. *Polymer* **54**, 2199–2221. (doi:10.1016/j.polymer.2013.02.023)
5. Bain EC. 1924 The nature of martensite. *Trans. AIME* **70**, 25.

Downloaded from https://royalsocietypublishing.org/ on 14 July 2022

6. Miyazaki S, Imai T, Igo Y, Otsuka K. 1986 Effect of cyclic deformation on the pseudoelasticity characteristics of Ti-Ni alloys. *Metall. Trans. A* **17A**, 115–120. (doi:10.1007/BF02644447)
7. Duerig T, Pelton A, Stöckel D. 1999 An overview of nitinol medical applications. *Mater. Sci. Eng. A* **273–275**, 149–160. (doi:10.1016/S0921-5093(99)00294-4)
8. Cui J, Wu Y, Muehlbauer J, Hwang Y, Radermacher R, Fackler S, Wuttig M, Takeuchi I. 2012 Demonstration of high efficiency elastocaloric cooling with large ΔT using NiTi wires. *Appl. Phys. Lett.* **101**, 073904. (doi:10.1063/1.4746257)
9. Gall K, Maier HJ. 2002 Cyclic deformation mechanisms in precipitated NiTi shape memory alloys. *Acta Mater.* **50**, 4643–4657. (doi:10.1016/S1359-6454(02)00315-4)
10. Zhao T-x, Kang G-z, Yu C, Kan Q-h. 2019 Experimental investigation of the cyclic degradation of the one-way shape memory effect of NiTi alloys. *Int. J. Min. Metall. Mater.* **26**, 1539–1550. (doi:10.1007/s12613-019-1884-8)
11. Sofla AYN, Elzey DM, Wadley HNG. 2008 Cyclic degradation of antagonistic shape memory actuated structures. *Smart Mater. Struct.* **17**, 025014. (doi:10.1088/0964-1726/17/2/025014)
12. Falk F. 1980 Model free energy, mechanics and thermodynamics of shape memory alloys. *Acta Metall.* **28**, 1773. (doi:10.1016/0001-6160(80)90030-9)
13. Müller I, Xu H. 1991 On the pseudo-elastic hysteresis. *Acta Metall. Mater.* **39**, 263. (doi:10.1016/0956-7151(91)90305-K)
14. Lovey FC, Torra V. 1999 Shape memory in Cu-based alloys: phenomenological behavior at the mesoscale level and interaction of martensitic transformation with structural defects in Cu-Zn-Al. *Prog. Mater Sci.* **44**, 189. (doi:10.1016/S0079-6425(99)00004-3)
15. Otsuka K, Sakamoto H, Shimizu K. 1979 Successive stress-induced martensitic transformations and associated transformation psedoelasticity in Cu-Al-Ni alloys. *Acta Metall.* **27**, 585. (doi:10.1016/0001-6160(79)90011-7)
16. Ball JM, James RD. 1987 Fine phase mixtures as minimizers of energy. *Arch. Ration. Mech. Anal.* **100**, 13–52. (doi:10.1007/BF00281246)
17. Ball JM, James RD. 1992 Proposed experimental tests of a theory of fine microstructure and the two-well problem. *Phil. Trans. R. Soc. Lond. A* **338**, 389–450. (doi:10.1098/rsta.1992.0013)
18. Bhattacharya K, Kohn RV. 1996 Symmetry, texture and the recoverable strain of shape-memory polycrystals. *Acta Mater.* **44**, 529–542. (doi:10.1016/1359-6454(95)00198-0)
19. Zanzotto G. 1992 On the material symmetry group of elastic crystals and the born rule. *Arch. Ration. Mech. Anal.* **121**, 1–36. (doi:10.1007/BF00375438)
20. Basinski ZS, Christain JW. 1954 Crystallography of deformation by twin boundary movements in indium-thallium alloys. *Acta Metall.* **2**, 101–116. (doi:10.1016/0001-6160(54)90100-5)
21. Wechsler MS, Lieberman DS, Read TA. 1953 On the theory of the Formation of Martensite. *Trans. AIME J. Metals* **197**, 1503–1529.
22. Bowles JS, Mackenzie JK. 1954 The crystallography of martensite transformations i/ii. *Acta Metall.* **2**, 129. (doi:10.1016/0001-6160(54)90102-9)
23. Wayman CM. 1994 The phenomenological theory of martensite crystallography: Interralationships. *Metall. Mater. Trans. A* **25**, 1787–1795. (doi:10.1007/BF02649029)
24. Cui J *et al.* 2006 Combinatorial search of thermoelastic shape-memory alloys with extremely small hysteresis width. *Nat. Mater.* **5**, 286–290. (doi:10.1038/nmat1593)
25. James RD, Zhang Z. 2005 A way to search for multiferroic materials with 'unlikely' combinations of physical properties. In *Magnetism and structure in functional materials* (eds Antoni Planes, L Mañosa, Avadh Saxena), pp. 159–175. Berlin, Germany: Springer.
26. Zhang Z, James RD, Müller S. 2009 Energy barriers and hysteresis in martensitic phase transformations. *Acta Mater.* **57**, 4332–4352. (doi:10.1016/j.actamat.2009.05.034)
27. Chluba C, Ge W, Lima de Miranda R, Strobel J, Kienle L, Quandt E, Wuttig M. 2015 Ultralow-fatigue shape memory alloy films. *Science* **348**, 1004. (doi:10.1126/science.1261164)
28. Chen X, Srivastava V, Dabade V, James RD. 2013 Study of the cofactor conditions: conditions of supercompatibility between phases. *J. Mech. Phys. Solids* **61**, 2566. (doi:10.1016/j.jmps.2013.08.004)
29. Zarnetta R. 2010 *et al.* Identification of quaternary shape memory alloys with near-zero thermal hysteresis and unprecedented functional stability. *Adv. Funct. Mater.* **20**, 1917–1923. (doi:10.1002/adfm.200902336)

Downloaded from https://royalsocietypublishing.org/ on 14 July 2022

30. Srivastava V, Chen X, James RD. 2010 Hysteresis and unusual magnetic properties in the singular Heusler alloy $Ni_45Co_5Mn_40Sn_10$. *Appl. Phys. Lett.* **97**, 014101. (doi:10.1063/1.3456562)
31. Liu J, Gottschall T, Skokov KP, Moore JD, Gutfleisch O. 2012 Giant magnetocaloric effect driven by structural transitions. *Nature Mater.* **11**, 620–626. (doi:10.1038/nmat3334)
32. Delville R, Schryvers D, Zhang Z, James RD. 2009 Transmission electron microscopy investigation of microstructures in low-hysteresis alloys with special lattice parameters. *Scr. Mater.* **60**, 293–296. (doi:10.1016/j.scriptamat.2008.10.025)
33. Delville R, Kasinathan S, Zhang Z, Humbeeck JV, James RD, Schryvers D. 2010 Transmission electron microscopy study of phase compatibility in low hysteresis shape memory alloys. *Philos. Mag.* **90**, 177–195. (doi:10.1080/14786430903074755)
34. Song Y, Chen X, Dabade V, Shield TW, James RD. 2013 Enhanced reversibility and unusual microstructure of a phase-transforming material. *Nature* **502**, 85. (doi:10.1038/nature12532)
35. Ni X, Greer JR, Bhattacharya K, James RD, Chen X. 2016 Exceptional resilience of small-scale $Au_30Cu_25Zn_45$ under cyclic stress-induced phase transformation. *Nano Lett.* **16**, 7621–7625. (doi:10.1021/acs.nanolett.6b03555)
36. Chen X, Tamura N, MacDowell A, James RD. 2016 *In-situ* characterization of highly reversible phase transformation by synchrotron X-ray Laue microdiffraction. *Appl. Phys. Lett.* **108**, 211902. (doi:10.1063/1.4951001)
37. Zhao ZX, Ma X, Cao S, Li YY, Zeng CY, Wang DX, Yao X, Deng ZJ, Zhang XP. 2020 Identification of nano-width variants in a fully monoclinic martensitic Ni50Ti50 alloy by scanning electron microscope-based transmission Kikuchi diffraction and improved groupoid structure approach. *Mater. Lett.* **281**, 128624. (doi:10.1016/j.matlet.2020.128624)
38. Li Z, Zhang Y, Esling C, Zhao X, Zuo L. 2011 Determination of the orientation relationship between austenite and 5M modulated martensite in Ni–Mn–Ga alloys. *J. Appl. Crystallogr.* **44**, 1222–1226. (doi:10.1107/S0021889811043366)
39. Li ZB, Zhang YD, Esling C, Zhao X, Zuo L. 2011 Determination of the orientation relationship between austenite and incommensurate 7M modulated martensite in Ni–Mn–Ga alloys. *Acta Mater.* **59**, 2762–2772. (doi:10.1016/j.actamat.2011.01.015)
40. Chen X, Song Y, Tamura N, James RD. 2016 Determination of the stretch tensor for structural transformation. *J. Mech. Phys. Solids* **93**, 34–43. (doi:10.1016/j.jmps.2016.02.009)
41. Karami M, Tamura N, Yang Y, Chen X. 2020 Derived crystal structure of martensitic materials by solid–solid phase transformation. *Acta Crystallogr. A* **76**, 521–533. (doi:10.1107/S2053273320006087)
42. Bhattacharya K, Conti S, Zanzotto G, Zimmer J. 2004 Crystal symmetry and the reversibility of martensitic transformations. *Nature* **428**, 55–59. (doi:10.1038/nature02378)
43. Pitteri M, Zanzotto G. 2002 *Continuum models for phase transitions and twinning in crystals*. Boca Raton, FL: CRC Press.
44. Friesecke G, James RD, Müller S. 2002 A theorem on geometric rigidity and the derivation of nonlinear plate theory from three-dimensional elasticity. *Commun. Pure Appl. Math.* **55**, 1461. (doi:10.1002/cpa.10048)